RESEARCH ARTICLE | MAY 15 2024

The advancing wave front on a sloping channel covered by a rod canopy following an instantaneous dam break \odot

Special Collection: Flow and Plants

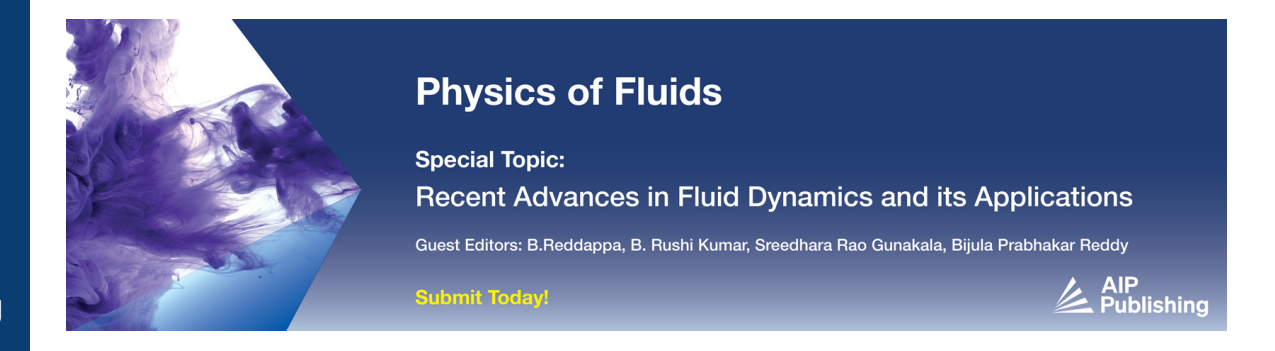
Elia Buono 🕶 💿 ; Gabriel G. Katul 💿 ; Davide Poggi 💿



Physics of Fluids 36, 054112 (2024) https://doi.org/10.1063/5.0209188









The advancing wave front on a sloping channel covered by a rod canopy following an instantaneous dam break

Cite as: Phys. Fluids **36**, 054112 (2024); doi: 10.1063/5.0209188 Submitted: 19 March 2024 · Accepted: 23 April 2024 · Published Online: 15 May 2024











AFFILIATIONS

¹Dipartimento di Ingegneria dell'Ambiente, del Territorio e delle Infrastrutture, Politecnico di Torino, 10129 Torino, Italy

Note: This paper is part of the special topic, Flow and Plants.

a) Author to whom correspondence should be addressed: elia.buono@polito.it

ABSTRACT

The drag coefficient C_d for a rigid and uniformly distributed rod canopy covering a sloping channel following the instantaneous collapse of a dam was examined using flume experiments. The measurements included space x and time t high resolution images of the water surface h(x, t) for multiple channel bed slopes S_o and water depths behind the dam H_o along with drag estimates provided by sequential load cells. Using these data, an analysis of the Saint-Venant equation (SVE) for the front speed was conducted using the diffusive wave approximation. An inferred $C_d = 0.4$ from the h(x, t) data near the advancing front region, also confirmed by load cell measurements, is much reduced relative to its independently measured steady-uniform flow case. This finding suggests that drag reduction mechanisms associated with transients and flow disturbances are more likely to play a dominant role when compared to conventional sheltering or blocking effects on C_d examined in uniform flow. The increased air volume entrained into the advancing wave front region as determined from an inflow-outflow volume balance partly explains the C_d reduction from unity.

Published under an exclusive license by AIP Publishing. https://doi.org/10.1063/5.0209188

I. INTRODUCTION

The sudden release of water following an instantaneous collapse of a dam has received much research attention in hydrology (e.g., overland flow), ecology (e.g., rapid inflow into wetlands or a marsh), hydraulics (e.g., flood routing), and coastal engineering (tsunami on coastal plains) for well over a century. 1-7 The hydrodynamics describing the unsteady and shallow nature of such flows are summarized by the Saint-Venant equation (SVE) introduced in 1871.^{8,9} For a rectangular prismatic section of constant width B, the SVE in their onedimensional form is given by two partial differential equations: the continuity and the area-averaged momentum balance. For the dambreak problem, the SVE is expressed as 1,10

$$\frac{\partial h}{\partial t} + \frac{\partial Uh}{\partial x} = 0 \tag{1}$$

and

$$\frac{\partial U}{\partial t} + U \frac{\partial U}{\partial x} + g \left(\frac{\partial h}{\partial x} + S_f - S_o \right) = 0, \tag{2}$$

where x is the longitudinal distance from the dam location with x = 0set at the dam location, t is time with t = 0 set to the instant the dam is removed, h(x, t) is the water depth, U(x, t) is the area-averaged or bulk velocity, g is the gravitational acceleration, S_o is the bed slope, and S_f is the friction slope that is unknown in the SVE. It is the closure model for S_f in the SVE that frames the scope of the work. As early as 1892, analytical results for the dam-break problem were derived when $S_f = 0$ and $S_o = 0.14,15$ The inclusion of finite S_o but keeping $S_f = 0$ revises the classical Ritter solution to 16

$$U(x,t) = \frac{2}{3} \left(\frac{x}{t} + U_o + S_o gt \right) \tag{3}$$

and

$$h(x,t) = \frac{1}{9g} \left(2U_o - \frac{x}{t} + \frac{1}{2} S_o g t \right)^2, \tag{4}$$

where $U_0 = \sqrt{gH_0}$ is the initial celerity speed. Here, the initial conditions to the SVE are a dry channel bed. When $S_0 = 0$ and t > 0, Eqs. (3) and (4) can be expressed in a dimensionless and compact form as

²Department of Civil and Environmental Engineering, Duke University, Durham, North Carolina 27708, USA

$$h_n = \frac{1}{9}(2 - u_n)^2, (5$$

where $h_n = h/H_o$ is the dimensionless water depth, $u_n = (x/t)(U_o)^{-1}$ is the dimensionless wave speed, $t_n = t(H_o/g)^{-1/2}$ is dimensionless time, and $x_n = x/H_o$ is dimensionless longitudinal position downstream from the dam. Revisions to these results are numerous and include a gradual breaching of the dam, ¹⁹ lateral contractions, ^{20–22} asymmetric geometry, ^{23–26} steep S_o , ^{15,27} and introduction of bends along the channel. ²⁸ Perhaps, the most studied revision to the inviscid solution is finite wall friction. ^{1,2,16,27,29–32} In prior applications with finite wall friction, a resistance formulation must be introduced to link S_f to the variables being modeled by the SVE (h or U). The primary restriction imposed on such models are recovering outcomes based on locally steady and uniform flow conditions. For these idealized flow conditions, the most common formulation to parameterize S_f is Manning's formula³³ that assumes a constant roughness coefficient (=n) and links S_f to the sought variables using

$$S_f = \left[\frac{2gn^2}{R_h^{4/3}} \right] \frac{U^2}{2g},\tag{6}$$

where $R_h = A_c/P_w$ is the hydraulic radius, $A_c = Bh$ is the cross-sectional area of the flow, $P_w = B + 2h$ is the wetted perimeter, and n is Manning's roughness coefficient (in s m^{-1/3} when SI units are used). This formulation is common given the accrued information on n over the years for different surface cover types. ^{11,34} Also, theoretical justification for Eq. (6) using turbulence theories and the energy cascade are also emerging. ^{35,36} In some applications, the kinematic wave approximation is invoked whereby the momentum balance is reduced to $S_f = S_o$. ³⁷ Invoking this approximation and inserting Eq. (6) into the continuity equation, a broad class of self-similar solutions can be derived and connections between the dam-break equations and the Fokker–Planck equations have already been proposed. ³ However, extending such solutions to the general SVE remains fraught with difficulties.

Controlled laboratory experiments on this topic remain also limited despite the undisputed societal significance of the dam-break problem. 16,17,38 Some laboratory studies considered (i) single isolated obstacles, $^{39-47}$ (ii) the initial stages of an instantaneous dam-break over smooth surfaces, $^{48-50}$ (iii) the use of polymer additives for inducing reductions in S_p^{51} (iv) geometric alterations to the channel section such as contractions, expansions, embankments, and bends, 20,21,28,52 and (v) the role of sediments and movable beds on S_p^{53-59} However, the dam-break problem for channels covered by vegetation remains under-studied with less than a handful being reported. 18 When the channel is vegetated, explicit inclusion of distributed drag into the SVE is necessary as energy losses are no longer related to wall friction. $^{60-69}$

The work here explores experimentally the effects of canopy drag on the physics of the advancing front following the instantaneous removal of a dam for varying static water depth H_o behind the dam and S_o . The canopy used is composed of staggered rigid cylinders covering the flume base downstream from a dam where S_o is varied from $S_o = 0\%$ to 3%. Attention is drawn to the role of canopy drag reduction mechanisms as the advancing front traverses the rod canopy. Thus, the two experimentally controlled variables to be manipulated here are S_o and H_o . A comparison with a prior study¹⁸ where the rod density was much higher is also presented.

II. THEORY

The setup considered here is for an instantaneous removal of a dam that results in a flood wave propagating downstream along a sloping rectangular channel. The channel is covered by a uniform rigid cylindrical rod canopy that acts to remove energy and momentum from the advancing flood wave. The cylinders are staggered and presumed to have a uniform diameter D and height $h_c/h(x,t)>1$ after the dam break. The goal is to describe the front position x_f and front speed U_f downstream from the dam for various combinations of control variables S_o and H_o . To arrive at an expression for S_f that accounts for the presence of cylinders to be used in the SVE, a starting point is to consider a *locally* steady-uniform flow within a canopy. The canopy is presumed to be sufficiently dense so that ground and sidewall friction contributions to the total stress can be ignored. Thus, a *local* balance between the gravitational contribution of the water weight along x and the drag resisting this motion results in

$$\rho g S_f V_w = \rho g C_d A_v \frac{U^2}{2g}, \tag{7}$$

where ρ is the water density, V_w is the water volume, A_v is the frontal area of the vegetation contained in V_w , and C_d is the drag coefficient. For the SVE, a force balance per unit ground area is preferred so that $V_w = h(1-\phi_v)$ and $A_v = mDh$, where ϕ_v is the solid volume fraction per ground area determined by $\phi_v = m\pi D^2/4$, m is the rod density (i.e., number of rods per unit ground area). This force balance leads to

$$S_f = \left[\frac{(C_d) \, mD}{1 - \phi_\nu} \right] \frac{U^2}{2g}. \tag{8}$$

Equations (6) and (8) can be made equivalent when introducing a non-constant Manning roughness given by

$$n = \sqrt{\frac{C_d m D}{2g(1 - \phi_v)}} R_h^{2/3}.$$
 (9)

Setting n to a constant value in models of S_f cannot be reconciled with a distributed drag formulation. The C_d which frames the scope of the work here, is influenced by numerous interactions between the canopy elements and the moving water. In steady-uniform flows, C_d is presumed to vary with Reynolds number $Re = VL/\nu$, where V and L are characteristic velocity and length scales respectively, and ν is the water kinematic viscosity. A number of possibilities have been introduced in the literature to define L and V in this context. Some set L to be proportional to D, rod spacing, or R_h . Likewise, V was set to pore-scale velocity, the constricted velocity, or a separation velocity. Ocrrections such as sheltering or blockage due to the presence of an array of cylinders have also been studied for an isolated cylinder and an array of cylinders.

Returning to the water level description in x and t of an advancing wavefront within a rod canopy, a number of simplifications have been adopted to the SVE. Within the wavefront region, the front speed attains a quasi-constant value so that the unsteady and inertial terms $\partial U/\partial t + U\partial U/\partial x$ are small relative to remaining terms. ¹⁶ For these standard simplifications, the SVE and the continuity equation become ¹⁸

$$g\left(\frac{\partial h}{\partial x} + S_f - S_o\right) = 0; \quad \frac{\partial h}{\partial t} + U\frac{\partial h}{\partial x} = 0.$$
 (10)

At very high Re, C_d may attain a quasi-constant value so that

$$U = \sqrt{-A\left(\frac{\partial h}{\partial x} - S_o\right)}, \quad A = \frac{2g(1 - \phi_v)}{C_d mD}.$$
 (11)

Inserting U into the approximated continuity equation and solving for h(x,t) results in

$$h(x,t) = C_1 + C_2 t + \frac{x}{3} [S_0 + E(S_0, A)], \tag{12}$$

where $E(S_o, A)$ is given by

$$E = \frac{R_1}{A} + \frac{AS_o^2}{R_1}, \quad \text{where}$$

$$R_1 = \left(A^3 S_o^3 - \frac{27A^2 C_2^2}{2} + \frac{3\sqrt{3}}{2} \sqrt{27A^4 C_2^4 - 4A^5 C_2^2 S_o^3}\right)^{1/3}. \quad (13)$$

Here, C_1 , and C_2 are integration constants independent of x or t. Equation (13) applies when $S_o > 0$. For $S_o = 0$, the solution to the simplified continuity and SVE system is ¹⁸

$$h(x,t) = C_1 + C_2 t - \left[C_2 \sqrt{\frac{C_d m D}{2g(1 - \phi_v)}} \right]^{2/3} x.$$
 (14)

It is to be noted that Eq. (14) is not recovered from Eq. (12) when setting $S_o = 0$ as this condition resembles a singular limit (i.e., addition of a new force). A near constant C_d implies h(x, t) is linear in x (and t) at

the advancing front region. The slope of this linear dependence on x varies with $C_d^{1/3}$ (i.e., sub-unity exponent).

III. EXPERIMENTS

The flume facility has been described in prior studies 18,75 and will not be fully repeated. Briefly, the tilting channel, the wooden cofferdam, the pneumatic pump release mechanism for the dam removal (mimicking an instantaneous dam break), the rod canopy, the water level imaging system, the load cells, the water level sensors, and the data acquisition system are featured in Fig. 1. The rectangular channel shown in this figure has a length L = 11.6 m, a width B = 0.51 m, and a side height $L_s = 0.6$ m. The channel sides are made of glass to allow imaging and optical access. The So was varied from 0% to 3%. The water behind the dam was filled until the target H_o is reached $(H_0 = 0.15, 0.20, 0.25, \text{ and } 0.30 \,\text{m})$. The quasi-instantaneous dam removal was carried out using a pneumatic pump that pulls rapidly the cofferdam vertically upward. After the dam removal, the water discharges from the end of the channel into a recirculating tank while passing over a rectangular weir. Downstream from the dam, an array of rigid cylinders of D = 0.006 and $h_c = 0.14$ m were used to represent the vegetation. The cylinders were fixed onto boards attached to the channel bottom and cover an entire cross section. A staggered rod configuration was used for all runs with a constant density $m = 190 \text{ rods m}^{-2}$.

To image h(x, t) during and after the dam removal, four synchronized Sony Handycam FDR-AX700 cameras were employed. The spatial resolution of each camera was 1920×1080 pixels interrogated in

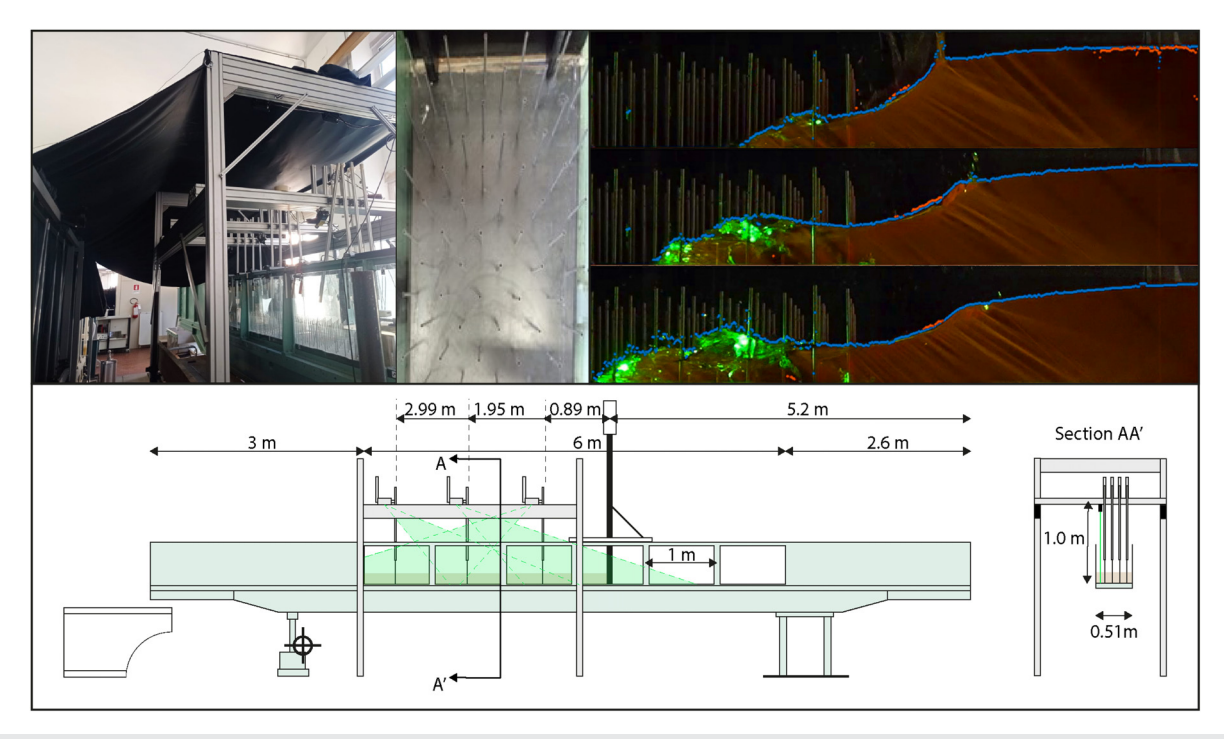


FIG. 1. The experimental setup for the dam break problem. On the top left, a picture of the channel downstream of the cofferdam and a top view of the rod canopy are featured. On the top right, three images from the early stages of the dam break wave propagation ($H_o = 0.15 \, \text{m}$, $S_o = 0\%$) are shown along with the detected free surface (blue dots). On the bottom, side view of the whole experimental facility (on the left) and longitudinal section view (on the right) with the most meaningful dimensions.

time at 100 frames per second. The cameras cover a total length of 4.2 m starting from 0.6 m behind the cofferdam. Such imaging configuration results in a pixel resolution of 1.07 mm. Water was mixed with a Rhodamine dye and a green laser plane was seated up parallel to the channel (55 mm from the left sidewall) to enhance the automated detection of h(x, t) and the delineation of the water surface profile. MATLAB (MathWorks, Natick, Massachusetts, USA) was used to analyze the movies by transforming the detected h(x, t) from pixel to metric coordinates as described elsewhere. 18 The detection of the free surface was based on a target color range in the HSV color system, meticulously adjusted for each test. Furthermore, alternative color systems, such as RGB, YCbCr, and Lab, were also tested but none yielded superior water level detection results when compared to the one used here. The duration of each experiment (i.e., a combination of H_0 and S_o) ranged from 5 to 10 s. Because air entrainment can modify the water level and need not be confined to the surface alone, the precise determination of h(x, t) from imaging is challenging. Thus, an uncertainty analysis was conducted on the water level detection scheme and is further discussed in the Appendix. The appendix derives variability by re-imaging the water level for each H_o - S_o combination three times.

The figures in the appendix present the standard deviation of the water level as well as the coefficient of variation of the longitudinal slope in the tip region for the three trials and for all H_o – S_o combination. The key findings from this appendix are that (i) the overall root-mean squared variability of the water level measurement (=2.3 mm) is commensurate with the pixel resolution (=1.07 mm) and (ii) the variability in water level detection had negligible impact on the longitudinal slope calculations needed for C_d .

Twelve load cells were used to record the drag force in t at 1 kHz on three downstream cross sections away from the dam ($X_{lc}=0.89$, 1.95, and 2.99 m). On each section, four load cells were placed with 0.1 m spacing starting at 0.05 m from the left side, according to the staggered canopy's pattern. The load cells used were eight Leane model DBBSM-1 kg-003-000 with accuracy of 3 μ N along with four Instrumentation Devices (model kD40s) with accuracy of 10 μ N. The drag F_d exerted on the instrumented rod is transferred to the load cell through a rigid active beam hinged on a fixed point as shown in Fig. 2. Each load cell was calibrated separately by applying a known force to the cell-beam system. The calibration procedure was conducted using five known loads per load cell and repeated for all slopes and load cells.

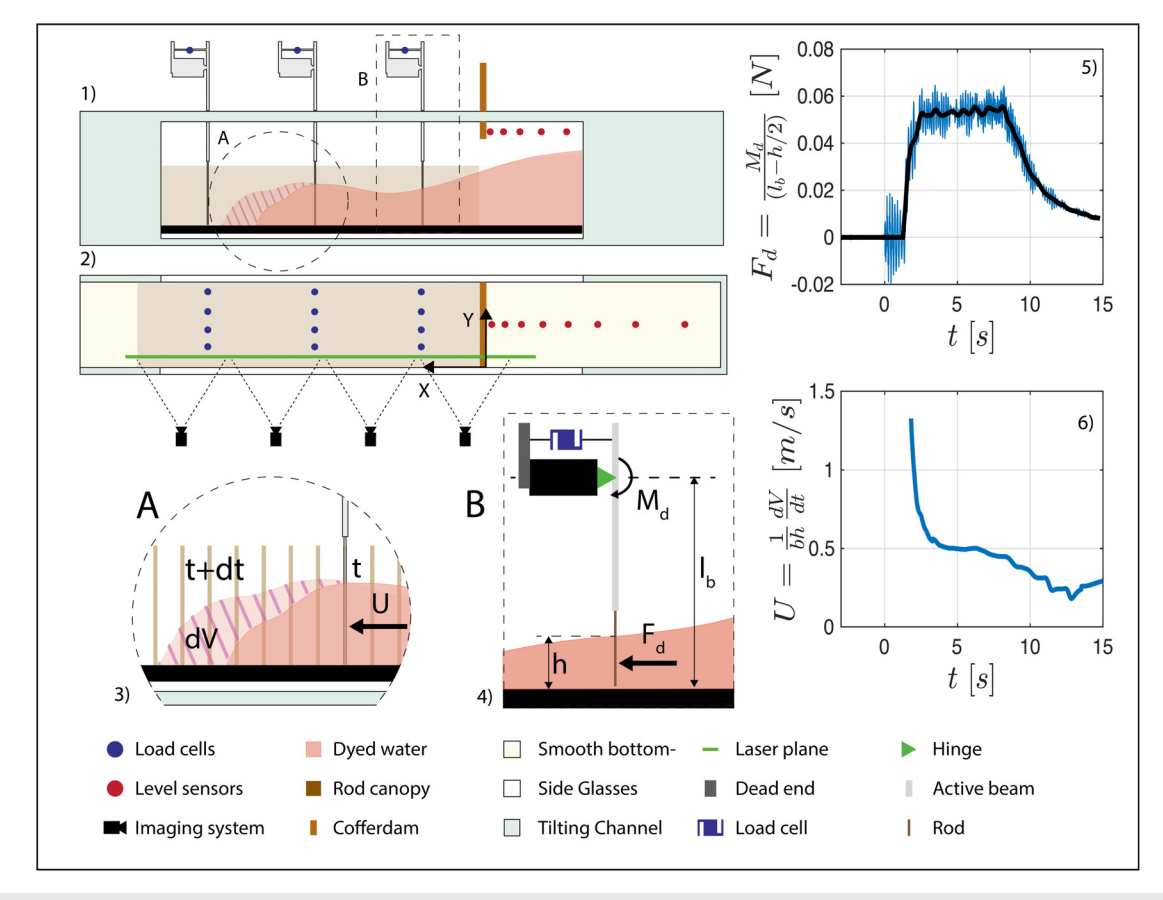


FIG. 2. A schematic of the instrument setup. (1) Side view of the channel with the dam released, (2) top view of the channel indicating the positions of the measuring instrumentation, (3) detailed view of the advancing wave front showing how the bulk velocity from imaged water depth was computed from water level measurements at time t and t+dt, (4) detailed view of the load cell system illustrating the method for drag measurements including the assumption of setting F_d at h/2, (5) a sample drag time series record in raw (blue line) and filtered (black line) form for $H_o = 0.15 \,\text{m}$, $S_o = 0\%$, $X_{lc} = 1.95 \,\text{m}$, and (6) the computed bulk velocity (blue line) for $H_o = 0.15 \,\text{m}$, $S_o = 0\%$, $X_{lc} = 1.95 \,\text{m}$.

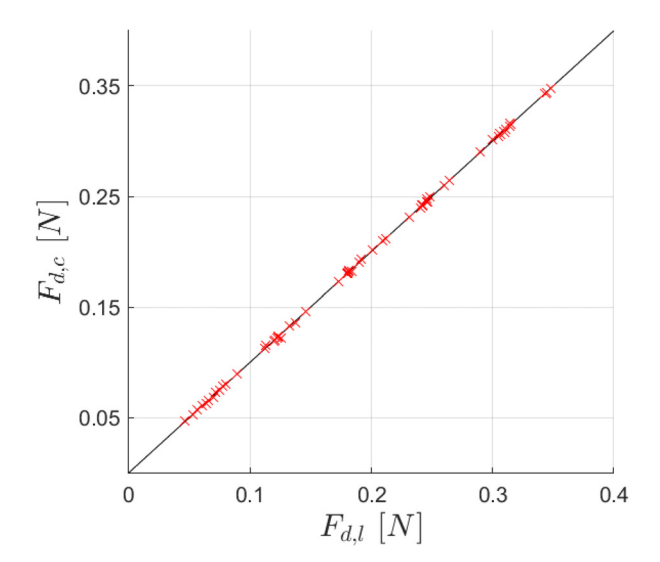


FIG. 3. Applied force during the calibration phase $F_{d,l}$ compared to the measured force obtained from the factory calibration curve $F_{d,c}$ for each of the 12 gauges. The calibration per gauge was carried out over five load values spanning the entire range of anticipated forces in the experiments. The illustration here refers to the $S_o=3\%$. The same procedure was repeated for all slopes.

TABLE I. Summary of the drag coefficient measurements from the load cells and from the friction slope S_f for steady-uniform flow (i.e., $S_f = S_o$) for different S_o . Here, the h is the mean water depth, Q is the discharge, U is the constricted cross section velocity, F_d is the mean drag measured by the load cells, $C_{d,p}$ is the drag coefficient determined from the load cells, $C_{d,f}$ is the drag coefficient determined from the uniform flow result with $S_f = S_o$ [i.e., Eq. (7)], and Re_d is, as before, the Reynolds number. The overall agreement between the C_d estimates by the two methods is better than 10% on average.

So (%)	h (m)	$Q\left(\mathrm{m}^3/\mathrm{s}\right)$	U(m/s)	$F_d(N)$	$C_{d,f}$	$C_{d,p}$	Re_d
1	0.08	0.016	0.42	0.037	1.00	0.87	2204
1	0.10	0.021	0.43	0.046	0.94	0.83	2266
1	0.12	0.026	0.45	0.069	0.85	0.93	2387
1	0.14	0.030	0.45	0.077	0.85	0.90	2380
2	0.06	0.017	0.60	0.061	0.96	0.95	3147
2	0.08	0.022	0.58	0.080	1.03	1.01	3038
2	0.10	0.029	0.60	0.105	0.94	0.97	3177
2	0.12	0.034	0.60	0.131	0.96	1.02	3142
2	0.14	0.040	0.59	0.156	0.99	1.07	3101
3	0.06	0.020	0.70	0.078	1.11	0.89	3672
3	0.08	0.028	0.73	0.113	1.01	0.88	3844
3	0.10	0.035	0.74	0.147	0.99	0.90	3882
3	0.12	0.043	0.75	0.184	0.97	0.92	3935
3	0.14	0.050	0.75	0.231	0.96	0.89	3943

The good performance of the factory calibration of the response force vs the applied force (five applied forces per load cell) for all 12 load cells is shown in Fig. 3 for the 3% slope. During the dam-break experiments, the torque onto the cell-beam system (= M_d) by F_d was recorded. The actual F_d was then derived assuming F_d is concentrated

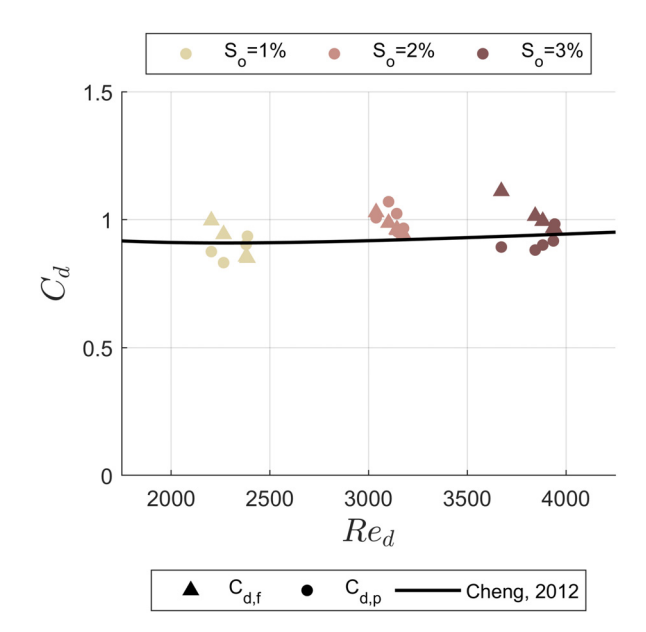


FIG. 4. The comparison between the drag coefficient C_d derived for an isolated cylinder, ⁷⁶ measured by the load cells $C_{d,p}$ and derived from friction slope $C_{d,f}$ using Eq. (7)—all presented as a function of Reynolds number Re_d for $S_f = S_o > 0$ when steady and uniform flow conditions are attained. The agreement between $C_{d,p}$ and $C_{d,f}$ support the assumption that wall friction can be ignored relative to the drag for such a rod density.

at half the depth $F_d = M_d/(l_b - h/2)$, where l_b is the distance from the channel bottom to the hinge. Additionally, eight level sensors (Balloff model BUS004W) were employed to record the water depth in t at 1 kHz behind the cofferdam. These sensors were located at the cross section center and spaced as $X_{ls} = -0.2, -0.4, -0.7, -1, -1.6, -2, -3$, and -4 m, where the free surface cannot be detected with the imaging system. An acquisition card (National Instruments, Austin, Texas, USA) was used for both load cells and level sensors. LabVIEW (National Instruments, Austin, Texas, USA) was used to drive data acquisition.

The C_d was quantified from the measured F_d using the quadratic drag-law $F_d=(1/2)C_d(Dh)U^2$. This quantification requires the bulk velocity on the instrumented cross section U_{lc} that was not directly measured. For each instrumented cross section X_{lc} , the U_{lc} was computed from measured h(x,t) using the continuity equation. Specifically, for each t the volume V_{lc} forwarding X_{lc} was computed by numerical integration of h(x,t) over x. The V_{lc} was then numerically differentiated to obtain the flow rate Q_{lc} through the instrumented section. The last step is to determine the bulk velocity from $U_{lc} = Q_{lc}/(h(x = X_{lc}, t)B)$. In Fig. 2, an illustration of how the bulk velocity was computed from this procedure is provided.

The dam-break experiments reported here were compared to prior experiments conducted in the same flume, same S_o-H_o combinations, and for the same staggered rod configuration. The main difference between the present and the prior experiments is the rod density m. In the prior experiments, $m = 1206 \, \text{rods m}^{-2}$ whereas here $m = 190 \, \text{rods m}^{-2}$. These prior experiments did not include load cell measurements or independent water level measurements behind the dam. Hence, their effective C_d was only inferred by fitting a numerical

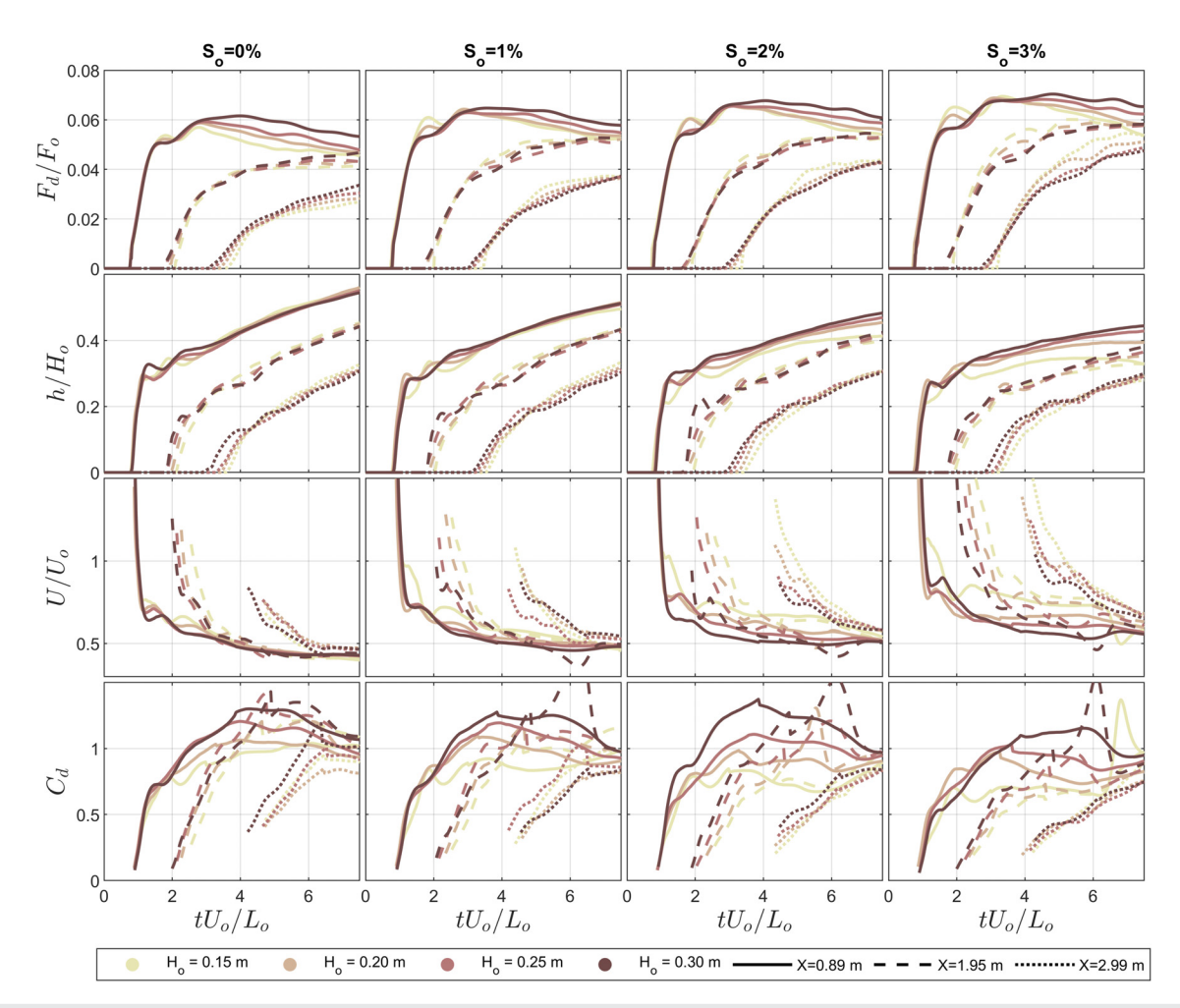


FIG. 5. Variations of the cross-sectional averaged normalized drag, water level, velocity, and C_d as a function of time at the three load cell locations for all H_o and S_o conditions (columns). Here, F_o is the normalizing force computed using $C_d = 1$, $U_o^2 = gH_o$, and $\rho = 1000 \text{ kg m}^{-3}$.

solution of the SVE to imaged h(x, t) for all the H_o – S_o combinations with assumptions about the inflow volume into the channel following the dam break. The most pertinent finding from these prior experiments was that a $C_d = 0.4$ better describes the measured h(x, t) than the numerous models proposed in the literature. ¹⁸

A separate experiment was also conducted here in the same channel to determine C_d for the steady and uniform flow case and for m=190. In these experiments, the staggered cylinder configuration was the same. The three target $S_o>0$ values were also used. The C_d for these experiments determined from the load cells $C_{s,p}$ and separately from Eq. (7) when setting $S_f=S_o$ are shown in Table I for completeness. In both cases, C_d was computed using the constricted cross section velocity $U_c=U/(1-\sqrt{2\phi_v/\pi})$.

IV. RESULTS AND DISCUSSION

To address the study objectives, this section is organized as follows. A comparison between measured C_d for steady-uniform flow cases and dam-break cases for all S_o values is presented. The magnitude and controls on C_d for this rod configuration for steady-uniform

flow can be used to ascertain whether wall friction can be ignored relative to the canopy drag and whether C_d estimates from the load cells match the expectations from Eq. (8). Next, the effects of H_o , S_o , and S_f on the wavefront are considered. These considerations are also used to summarize the data from the experiments in a normalized manner. Once again, data from the prior study (m = 1206) and the present experiments (m = 190) are compared to assess the effects of $C_d mD$ on S_f . To facilitate comparisons across the $H_o - S_o$ cases and the two mvalues, a single reference curve was repeated in all of them based on Eq. (5). This "baseline" curve makes a logical choice for a reference because it is derived for $S_f = 0$ and $S_o = 0$. The physics of the advancing front wave is considered next. Two regimes are shown to emerge when analyzing the measured front position x_f against estimates from $U_o t$. The first is a rapid regime dominated by both inertial and frictional effects, and a second regime trending toward the diffusive wave approximation where the frictional effects experience a reduced C_d . A discussion as to the possible causes of this drag reduction is then offered. Throughout, the results in the figures are presented in dimensionless form using the following: water depths are normalized by H_0 ,

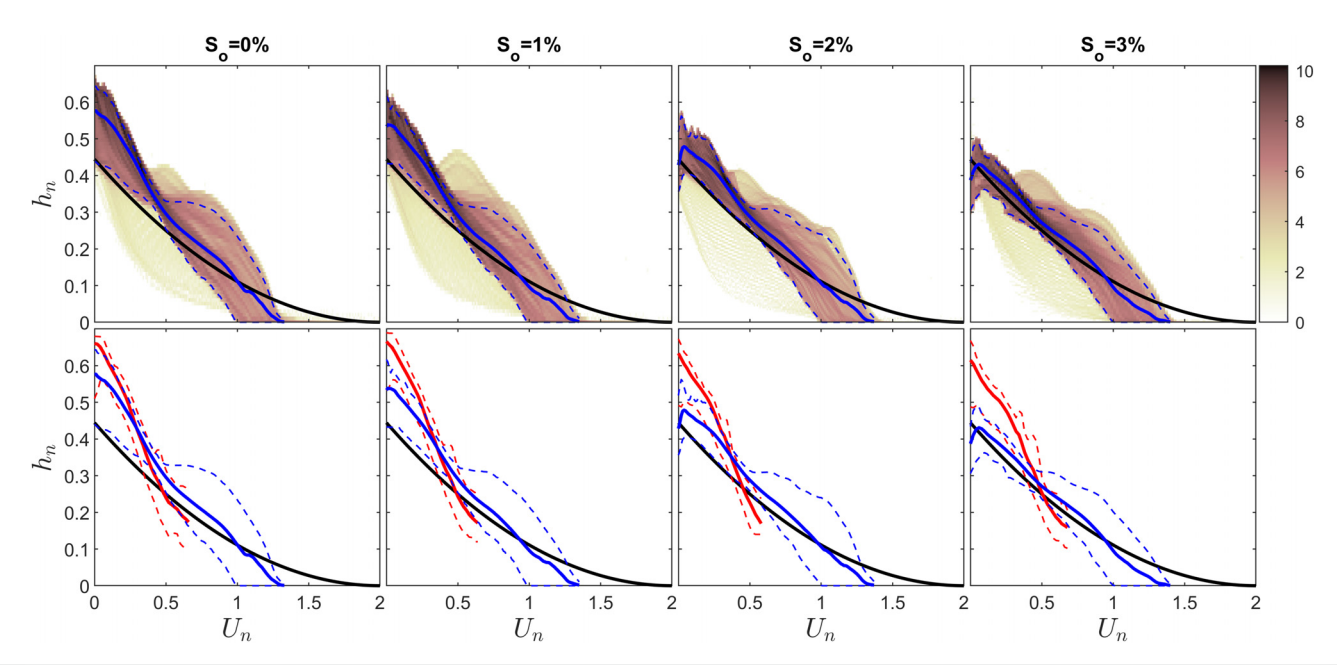


FIG. 6. The measured normalized water depth $h_n = h/H_0$ (ordinate) variations with the normalized velocity $U_n = (x/t)/U_0$ (abscissa) along with the Ritter solution (black solid line) for all four bed slopes S_o . In the top panels, the blue lines represent the derived h_n (solid line) and the 95% confidence bound (dashed lines). The color scale is featured to show the $log_{10}(N)$ data points used in the derivation of $h_n - U_n$ relation. The bottom panels repeat the blue lines (m = 190) from above and add earlier experiments (m = 1206) for the dense rod density case¹⁸ (red lines).

velocities are normalized by U_o , time is normalized by U_o/L_o , where $L_o = (C_d m D)^{-1}$ is a reference adjustment length⁷⁷ taken at $C_d = 1$ (i.e., steady-uniform flow case), forces are normalized by $(1/2)C_d\rho DH_oU_o^2$ and horizontal distances are normalized by L_o .

A. Drag coefficient from the load cells

For steady-uniform flow, the measured C_d from the load cells $C_{d,p}$ and from friction slope $C_{d,f}$ shown in Fig. 4 do not deviate significantly from the accepted formulation for an isolated cylinder $C_{d,iso}$ that is given by Cheng⁷⁶ and Wang *et al.*⁷⁸

$$C_{d,iso} = 11(Re_d)^{-0.75} + 0.9\Gamma_1(Re_d) + 1.2\Gamma_2(Re_d),$$
 (15)

where $Re_d = U_c D/\nu$ is the element Reynolds number and

$$\Gamma_1(Re_d) = 1 - \exp\left(-\frac{1000}{Re_d}\right),$$

$$\Gamma_2(Re_d) = 1 - \exp\left[-\left(\frac{Re_d}{4500}\right)^{0.7}\right].$$
(16)

This expression assumes that $Re_d < 10^4$ (and is below the drag crisis range for isolated cylinders) and that the drag from each cylinder operates in isolation (i.e., no interference, sheltering, or blocking). The agreement between $C_{d,p}$ and $C_{d,f}$ is also suggestive that wall friction that impacts $C_{d,f}$ but not $C_{d,p}$ can be ignored relative to the canopy drag for such a rod density. In the range of Re_d considered here, a $C_d = 0.9 - 1.1$ appears to describe the steady-uniform flow data without any significant dependency on Re_d as shown in Fig. 4. For this reason, the reference drag $C_d = 1$ is selected in the L_c calculations used for normalizing longitudinal distances. Returning to the dam-break cases,

the load cell measured F_d was used, together with the imaged water depth h, to compute C_d using $F_d=(1/2)C_d\rho DhU^2$. Here, the U was computed from the continuity equation using the imaged water depth as shown in Fig. 5. The computed C_d is well below unity as the wave front passes. This reduction in C_d is significant for all S_o values. For early times $t(U_o/L_o) < 1$, C_d increases from some 0.2-0.6 as shown in Fig. 5 with a mean of about $C_d=0.4$. The mean value here is consistent with the value inferred indirectly from fitting the SVE to measured h(x,t) in the prior study despite the large difference in m between the two experiments. The agreement between the reduced drag value $(C_d=0.4)$ across the two experiments hints that sheltering alone may not be the main mechanism responsible for drag reduction as sheltering is expected to dependent on rod density.

B. Bed slope and frictional effects

To illustrate the simultaneous effects of S_o and H_o variations on the depth-velocity relations, the experiments here (m=190) are summarized in Fig. 6 and then compared to Eq. (5) for $S_o=S_f=0$. The prior experiments for m=1206 are also added for reference and are organized, as before, by the two control variables S_o and H_o . A number of comments can be made about Fig. 6.

- Equation (5) over-predicts the advancing front wave speed (i.e., the U_n associated with $h_n < 0.05$) for all $S_o H_o$ cases compared to their frictional counterparts as expected.
- The higher m experiments result in higher water pile-up (i.e., higher h_n) at the smaller $U_n < 0.5$ values as expected.
- With increasing S_o , the lower m data approach Eq. (5) (i.e., the solution for $S_o = S_f = 0$) except for the advancing wave front region. This finding may be explained by the fact that increasing

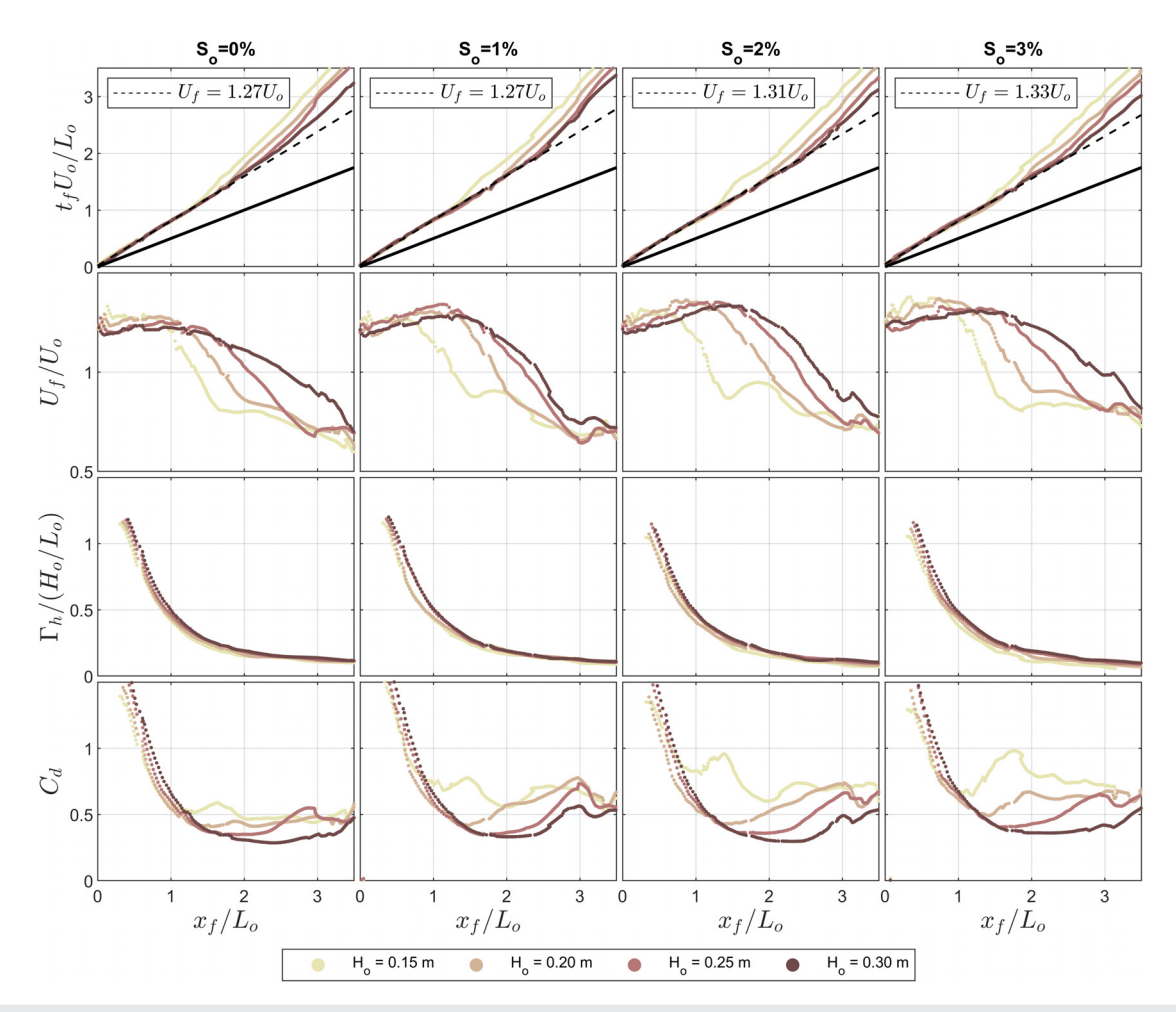


FIG. 7. The relation between wave front position x_f and those determined when assuming $x_f = U_o t$ from the top to the bottom: the time t_f multiplied by the characteristic velocity U_o , the normalized wave front velocity U_f/U_o , the tip slope $\Gamma_h = -\partial h/\partial x$ divided by characteristic depth H_o , and the inferred drag coefficient C_d using the diffusive wave approximation.

 S_o also increases S_f thereby diminishing their difference in the SVE (S_f is always finite and large in the presence of a canopy). The advancing front (i.e., the region with $h_n < 0.05$) always experiences a slow-down (lower U_n) compared to Eq. (5) as noted earlier.

In sum, Fig. 6 confirms all the logical expectations of the $u_n - h_n$ relations derived from the experiments for differing m values, S_o , and H_o . Common to all the cases is the slow-down for the advancing front region when compared to the $S_f = 0$ case due the canopy. In the absence of a canopy, the Ritter solution reasonably describes the advancing wavefront for the channel setup here as discussed elsewhere. The advancing front region is now explored in detail.

C. Two dynamical regimes

The dynamical regimes that introduce deviations from Eq. (5) are examined along x. These regimes are identified by exploring how the normalized front position x_f/L_o varies against tU_o/L_o as shown in

Fig. 7. Two distinct regimes can be identified with a transition governed by the initial H_o for all S_o (top panels). At small distances from the dam (first regime, $x_f/L_o < 1$), a robust $x_f = c_f U_o t$ can be seen from the experiments where $c_f = 1.26$ for $S_o = 0$ and $c_f = 1.33$ for $S_f = 3\%$. This implies that the advancing front velocity $U_f = c_f \sqrt{gH_o}$ is roughly a constant and weakly dependent on So given the small increase in c_f with increasing S_o . Setting x/t = U in Eq. (5) leads to a frictionless advancing front speed that is almost twice as fast (i.e., $c_f = 2$ for $S_f = S_o = 0$) as discussed elsewhere. Beyond a near constant U_f for $x_f/L_o < 1$, another dynamically interesting feature of this regime is the rapid drop in measured $\partial h/\partial x$ with increasing x_f until the attainment of the second regime $x_f/L_o > 1$. The second regime marks a gradual slow-down in U_f/U_o compared to the near-constant velocity in the first regime (top two rows in Fig. 7), but trends toward a near constant $\Gamma_h = -\partial h/\partial x$ with increasing x_f/L_o . Thus, while the first regime experiences a near constant U_f and a variable Γ_h , the second regime is dynamically the opposite. The increase in H_o delays the onset of the slow down (or second) region with increased x_f (i.e., reduced U_f)

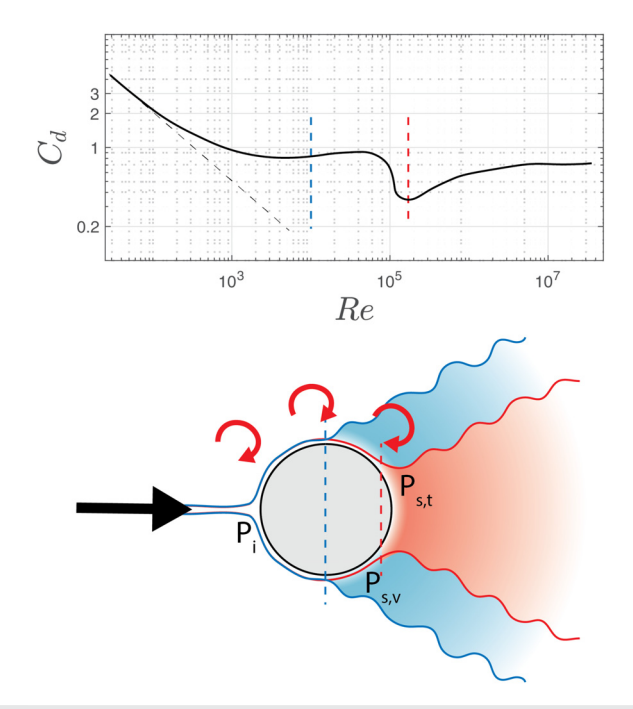


FIG. 8. Conceptual model for the boundary layer detachment from a cylinder during the drag crisis (red wake, boundary layer is turbulent) compared with pre-crisis (blue wake, boundary layer is laminar). The delayed separation during the drag crisis has two effects: (i) it allows for a pressure recovery (i.e., $P_{s,t}$ is less negative than $P_{s,v}$ shown at the dashed blue centerline of the cylinder), thereby reducing the pressure difference between the front (P_i) and back of the cylinder (i.e., $P_{s,v}$ or $P_{s,t}$), and (ii) it reduces the wake area behind the cylinder (red vs blue). Both effects act in concert to reduce the form drag C_a shown on top as a function of Re. The dashed vertical lines show the Re for the pre-crisis (blue) and during the drag crisis (red).

for all S_o values. It is expected that with further increases in x_f/L_o , U_f/U_o , $\Gamma_h L_o/H_o$, and likely C_d all attain a constant value in agreement with the diffusive wave approximation. The measurements reported in Fig. 7 seem to support this extrapolation for the low H_o cases considered.

The fact that U_f varies may appear counter to the approximated physics in Eq. (10). However, a detailed analysis (not shown here) conducted on the data suggest that

$$\frac{\partial Uh}{\partial x} \approx U_f \frac{\partial h}{\partial x}; \quad \left| \frac{\partial U}{\partial t} + U \frac{\partial U}{\partial x} \right| \ll \left| \frac{\partial h}{\partial x} \right|.$$
 (17)

Thus, the diffusive wave approximation remains plausible in the second regime despite variations in U_f with x_f .

Returning to the drag reduction issue, a C_d was inferred from Eq. (11) using measured U_f and measured $\partial h/\partial x$ for the $S_o - H_o$ combinations. These computed C_d values are shown in Fig. 7. To be clear, the estimate of C_d using a diffusive wave approximation for the first region (i.e., $x_f/L_o < 1$) cannot be correct. The computed C_d is only presented here to corroborate the transition zone from the first to the second region around $x_f/L_o = 1$, where the diffusive wave approximation begins to apply for $x_f/L_o > 1$. Beyond that x_f a near constant C_d is attained from Eq. (11). The low C_d values measured by the load cells shown in Fig. 5 agree with those computed from the diffusive wave approximation using measured h(x, t). This agreement in reduced C_d for the second region serves two purposes: (i) it shows that the diffusive wave approximation is plausible for $x_f/L_o > 1$, and (ii) it confirms that a new drag reduction mechanism must be operating that is unique to the dam-break problem (i.e., it does not exist in the steady-uniform flow cases).

D. What causes the drag reduction?

To recap the findings thus far, the m=1206 experiments yielded a $C_d=0.4$ inferred from h(x,t) measurements by fitting an optimum C_d to the SVE so as to match h(x,t). It was postulated that this fitted and reduced drag is linked to the so-called drag crises. ¹⁸ For an isolated cylinder immersed in a steady and uniform background flow that describes its far-field, the drag crisis occurs when well-organized vortex shedding (e.g., Karman-vortex streets) are disrupted and transition to randomized shedding with further increases in Re_d . ⁷⁹ This transition occurs at very large Re_d (>10⁵) in the isolated cylinder case and for steady-uniform flow as shown in Fig. 8. Numerical simulations confirm that the drag crisis commences when a critical Reynolds number

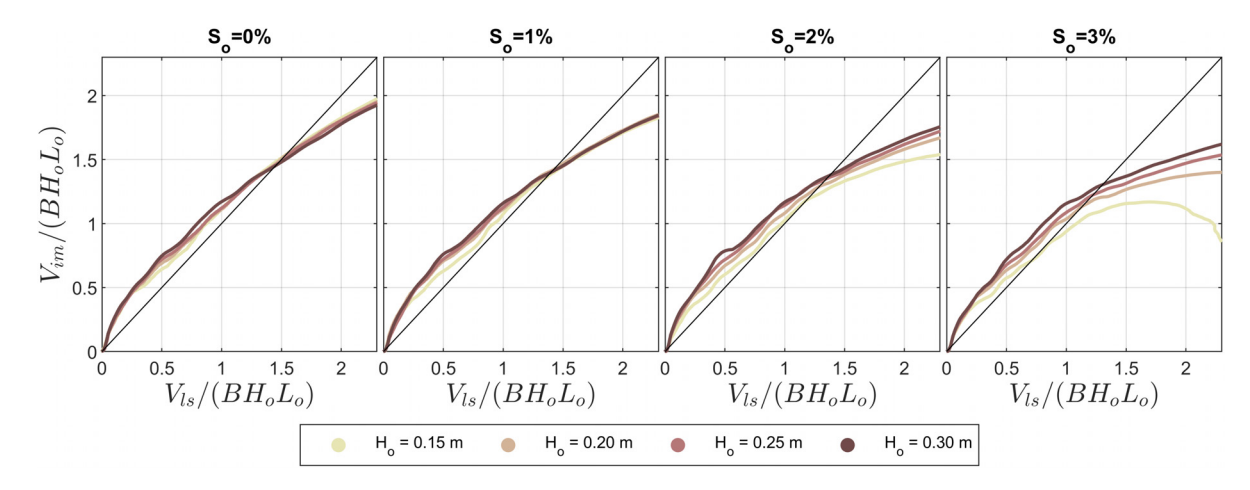


FIG. 9. A comparison between normalized water volume within the channel for t > 0 from the imaging system (ordinate) for x > 0 and from level sensors (abscissa) behind the dam x < 0.

is reached where the boundary layer on the cylinders become turbulent thereby maintaining attachment to the cylinder further downstream. The transition to a turbulent boundary layer and a sustained attachment onto the cylinder has two effects. The first is that the pressure differential between the front (P_i) and the back $(P_{s,t})$ for turbulent vs $P_{s,v}$ for laminar) of the cylinder is reduced due to the partial pressure $(P_{s,t} > P_{s,v})$ recovery following a longer downstream attachment⁸⁰ along the back of the cylinder as schematized in Fig. 8. Numerical simulations for an isolated cylinder with a uniform far field flow have shown that this pressure recovery does occur because of delayed separation on the back of the cylinder and can reduce the pressure differential (referenced to P_i) by more than 25%. The second is that the wake area is also reduced (red vs blue shades in Fig. 8) as detailed by simulations. 79,80 The combined effect of reduced pressure differential and reduced wake area leads to a drastic reduction in C_d (more than a factor of 2)—or the drag crisis.

It was conjectured in the prior study 18 that the dam-break problem leads to a disturbed and transient "far-field" background flow region that enables the randomization of vortex shedding to be initiated and persistent at much lower Re_d . This disturbed far-field state can enhance momentum transport to the turbulent boundary layer region attached onto the cylinder and allows the drag crisis to be maintained as schematized in Fig. 8. A reduced C_d is then to be sustained over an extended range of Re_d well below the critical value of $Re_d = 10^5$ (where the laminar boundary layer flips to a turbulent state for an undisturbed background state).

The work here offers an amendment to this argument, which is the air entrainment leading to density reductions at the advancing front in the second region as shown in the photographs of Fig. 1. Figure 9 presents a comparison between the measured normalized volume of the inflow behind the dam using water level sensors (ordinate) and the imaged volume of water as the front progresses downstream from the dam for x/t > 0 (abscissa). Noting that $x_f \approx 1.3 U_o t$ in Fig. 7 and that the test section region analyzed in Fig. 7 is for $x_f/L_o \le 3$, it is clear that the imaged outflow volume appears to be consistently larger by some 10%-20% compared to the inflow volume (i.e., volume behind the dam measured by detailed water level measurements). From an experimental uncertainty point of view, the splashing and breakup of water into fine droplets near the advancing tip region shown in Fig. 1 would have reduced, not increased, the imaged outflow volume. Water droplets, which are not counted in the imaged h(x, t)volume calculations, will be missed. Since water mass is conserved, the imaged outflow volume exceeding the inflow volume must then be associated with some air entrained at the advancing front. With air volume entrained at the advancing wave front region, the overall water density near the tip front must be substantially reduced. A reduction in water density near the advancing front region leads to a concomitant overall inferred F_d and C_d reductions in this vicinity. This drag reduction mechanism may be acting in concert with the randomization of vortex shedding associated with the earlier speculated drag crisis. 18 Thus, air entrainment, reduced water density at the advancing front region, and a disturbed background state all conspire to reduce C_d by a factor of 2.

V. CONCLUSIONS AND BROADER IMPLICATIONS

The closure of the friction slope in the SVE continues to draw research attention as it encodes all the solid–fluid interactions. In operational models of flood waves, the S_f is related to $U^2/(2g)$ using

conventional formulations that aim to recover the steady-uniform flow (e.g., Manning's formula). However, the presence of drag elements adds another layer of complexity and that cannot be represented as an equivalent wall friction derived using steady-uniform flow conditions. Those interactions are represented by a drag coefficient C_d that modifies S_f as shown here. As before, steady-uniform flow are assumed as baseline state to link C_d to S_f in practice. This approach was deemed pragmatic in many dam break and flood routing applications, because there are numerous datasets and models for C_d when the drag elements are rod canopies (or other approximated geometries). Much research has focused on corrections to C_d from an isolated cylinder and include sheltering, blockage, among others. The work here suggests that C_d from steady-uniform flow may be an overestimate by a factor of 2. New physics at the advancing front related to air entrainment and randomization of coherent vortex structures occur due to the unsteady and disturbed nature of the flow away from the rod canopy. These two effects act as drag reduction mechanisms that "speed up" the advancing front relative to C_d models derived from steadyuniform flow.

The work also identified two dynamically interesting regimes for the advancing front velocity based on where the front location x_f is relative to the adjustment length scale $L_o = (C_d m D)^{-1}$. For $x_f/L_o < 1$, the front velocity is roughly constant and scales with $\sqrt{gH_o}$ and $\partial h/\partial x$ rapidly declines in magnitude. A second regime for $x_f/L_o > 1$ emerges where the front velocity begins to decline but $-\partial h/\partial x$ begins to attain its minimum. The diffusive wave approximation further suggests that in the second regime, the drag coefficient is reduced by a factor of 2 relative to its steady-uniform value.

This work must be viewed as an embryonic step so as to improve flood forecasting in the future. Additionally, the present results offer benchmark data for future numerical investigations given the increased focus on modeling and simulating dam-break problems^{61,81–86} over obstructions and vegetated bed scenarios.⁸⁷ need to move beyond wall friction representation for energy losses is recognized in large scale models but alternatives remain in short supply. 18 Progress on these alternatives using a quadratic drag law is timely given the rapid advancements in water level measurements from space (to within 10 cm)⁹¹ and the wealth of research on drag coefficients for different geometries as derived from steady-uniform flow. However, the disturbed and transient nature of this flow was shown to lead to previously unexplored drag reduction mechanisms (air entrainment, drag crisis). Future experiments should seek novel methods to characterize the water density reductions and the randomization of vortex shedding associated with the drag crisis for such disturbed flows. From the simulation perspective, the results here hint that a three-phase representation (solid, water, and air) may be needed to capture the interplay between air entrainment and boundary layer separation at the solid interface of the cylinders during the dam break.

ACKNOWLEDGMENTS

E.B. acknowledges Politechnico di Torino (Italy) for supporting the visit to Duke University. G.K. acknowledges support from the U.S. National Science Foundation (No. NSF-AGS-2028633) and the U.S. Department of Energy (No. DE-SC0022072). D.P. acknowledges support from Fondo europeo di sviluppo regionale (FESR) for project Bacini Ecologicamente sostenibili e sicuri, concepiti per l'adattamento ai Cambiamenti ClimAtici

(BECCA) in the context of Alpi Latine COoperazione TRAnsfrontaliera (ALCOTRA), and project Nord Ovest Digitale e Sostenibile – Digital innovation toward sustainable mountain (Nodes – 4).

AUTHOR DECLARATIONS Conflict of Interest

The authors have no conflicts to disclose.

Author Contributions

Elia Buono: Conceptualization (equal); Data curation (equal); Formal analysis (equal); Methodology (equal); Writing – original draft (equal). Gabriel G. Katul: Conceptualization (equal); Methodology (equal); Supervision (equal); Writing – original draft (equal). Davide Poggi: Conceptualization (equal); Funding acquisition (lead); Methodology (lead); Supervision (lead); Writing – review & editing (equal).

DATA AVAILABILITY

The data that support the findings of this study are available from the corresponding author upon reasonable request.

APPENDIX: WATER SURFACE DETECTION ACCURACY

In shallow water flow such as the one encountered during a dam break with canopies, air entrainment is expected. The entrainment is largely a diffuse phenomenon and leads to a rise in the free water surface as well as a reduction in the bulk density. Typically, the distribution of air entertained within the volume of water and, consequently, the upward movement of the free surface have random behavior in space. In this Appendix, an uncertainty analysis is conducted on the water level detection to assess its uncertainty as well as offer additional clarification about the free surface detection methodology and its limits.

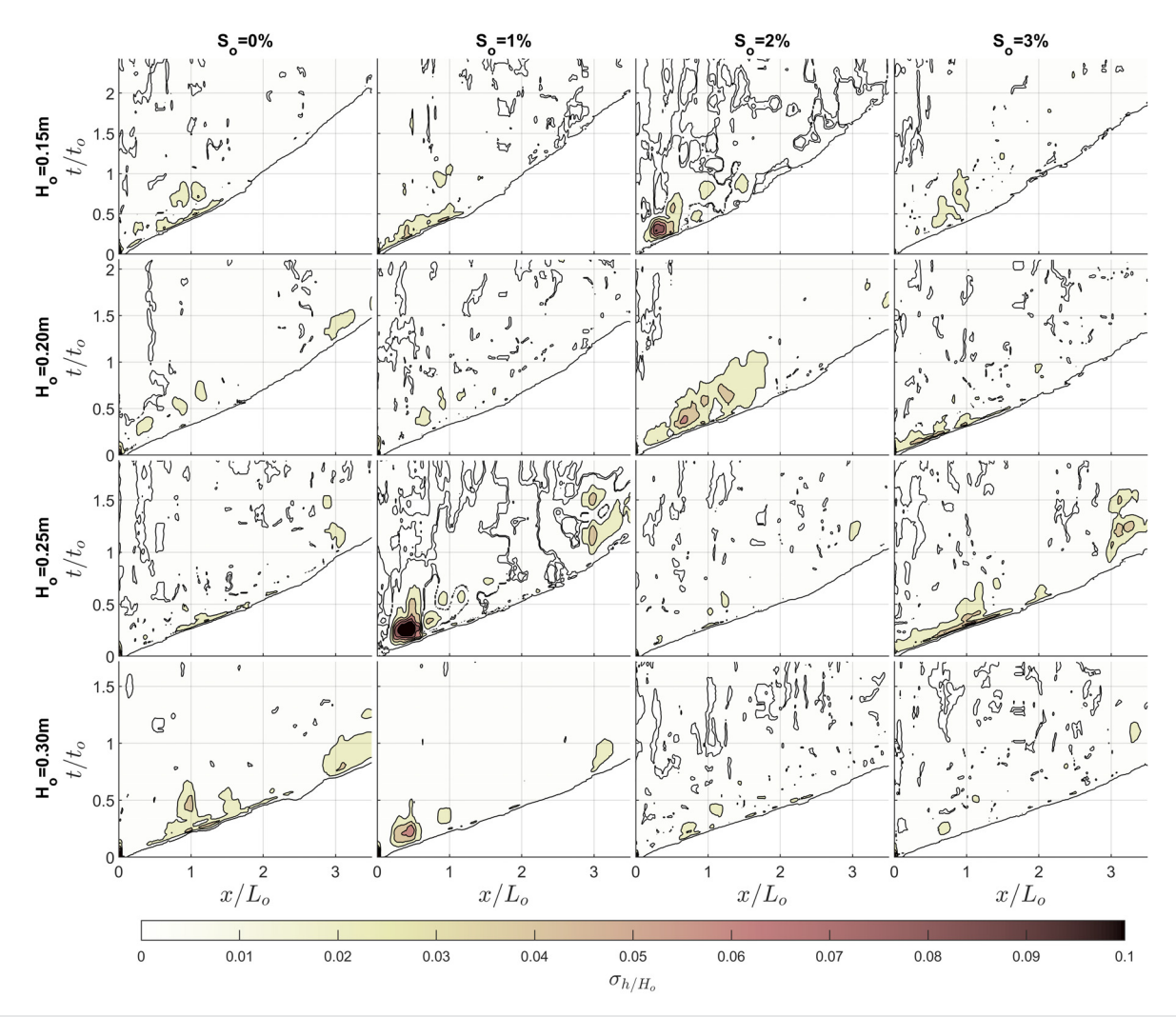


FIG. 10. Standard deviation of normalized depth σ_{h/H_0} as function of normalized distance x/L_0 and normalized time t/t_0 with $t_0 = \sqrt{H_0/g}$ for all the experimental conditions (levels at $\sigma_{h/H_0} = 0.001, 0.02, 0.04, 0.06, 0.08,$ and 0.1).

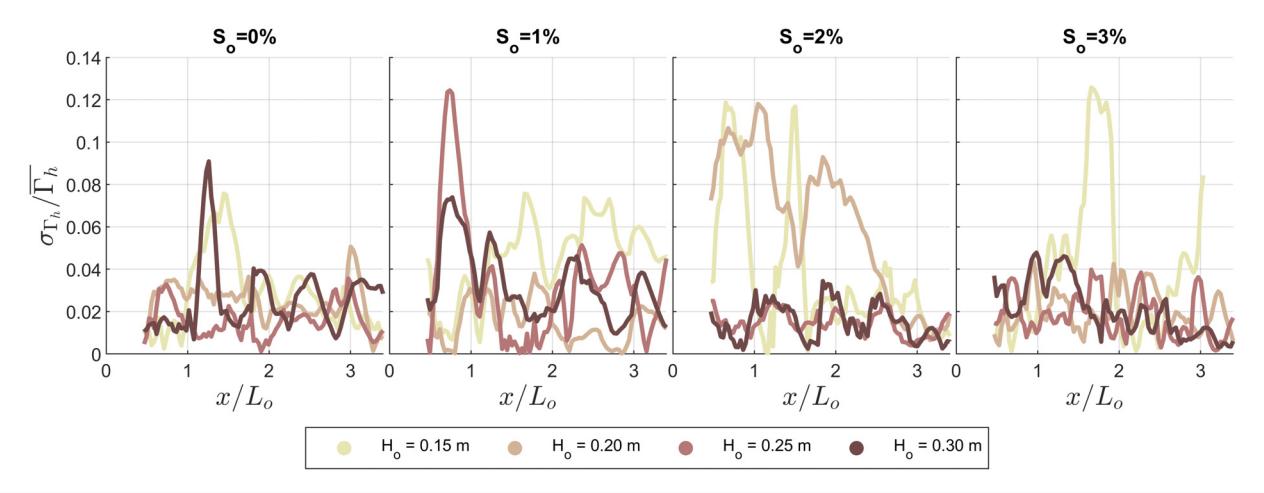


FIG. 11. Coefficient of variation of the tip slope $\sigma_{\Gamma_h}/\Gamma_h$, where $\Gamma_h=-\partial h/\partial x$. These coefficients of variations were obtained based on standard deviation and mean derived for the regression slopes of each of the three trials.

The imaging technique here is based on the ability of Rhodamine dye to emit light in a specific wavelength when excited by a laser. The interaction between Rhodamine dye and the laser leads to a characteristic shade of red that can be isolated digitally by color identification. However, regions in the volume of water with high concentration of bubbles reflect and diffuse the laser light, resulting in bright green colors. An increase in the color range to accommodate bright green regions can be conducted. However, this increase in light range leads to higher probability of miss-detection of the true water level, whatever this level may be. Attempting to filter out zones with air bubbles entrained within the entire water volume is an option, but this option leads to gross underestimation of the volume of water. Moreover, the variability in color do not allow distinguishing quantitatively air from water in the wave body, at least not with the imaging system used here. This limitation cannot be readily overcome with post-image processing and requires a far more sophisticated video acquisition technique such as equipping the cameras with filters to block the wavelength of the lasers' light.

The assessment here takes advantage of the aforementioned stochastic behavior of the free surface due to air entrainment that results in certain variability in the water depth (especially in the tip region). To quantify the magnitude of this variability, each combination of $H_o - S_o$ run has been repeated three times. The standard deviation of the normalized water depth h_n , depicted in Fig. 10, was then computed as well as the coefficient of variation of the advancing wavefront longitudinal slope Γ_h , also shown in Fig. 11.

The overall variability in water depth detection was computed by summing the variance on h in space and time and for each combination of H_o-S_o . The associated standard deviation for the h variability is 2.3 mm and is comparable with the pixel resolution (=1.07 mm). As can be seen in Fig. 10, the run-to-run standard deviation in h is typically lower than 0.02 away from the tip region and, as might be expected, increases in the tip region, especially in the initial stages, reaching values up to 0.1. Nevertheless, the higher variability in h within the tip region do not affect the tip slope determination. The analysis here shows that the coefficient of variation in the longitudinal slope is typically lower than 4% and never

exceeds 13%. This robustness is expected as regression analysis used to determine the longitudinal slope per run already averages out the stochastic nature of air entrainment effects in space on h(x, t). The slope values reported in the estimation of C_d are the ensemble-average of all three trials.

REFERENCES

- ¹G. B. Whitham, "The effects of hydraulic resistance in the dam-break problem," Proc. R. Soc. A **227**, 399–407 (1955).
- ²B. Hunt, "Asymptotic solution for dam-break problem," J. Hydraul. Div. 108, 115–126 (1982).
- ³E. Daly and A. Porporato, "Similarity solutions of nonlinear diffusion problems related to mathematical hydraulics and the Fokker-Planck equation," Phys. Rev. E **70**, 056303 (2004).
- ⁴H. Chanson, "Tsunami surges on dry coastal plains: Application of dam break wave equations," Coastal Eng. J. 48, 355–370 (2006).
- ⁵A. E. Ajayi, N. van de Giesen, and P. Vlek, "A numerical model for simulating Hortonian overland flow on tropical hillslopes with vegetation elements," Hydrol. Processes 22, 1107–1118 (2008).
- ⁶J. L. Carrivick, "Dam break-outburst flood propagation and transient hydraulics: A geosciences perspective," J. Hydrol. **380**, 338–355 (2010).
- ⁷S. Thompson, G. Katul, A. Konings, and L. Ridolfi, "Unsteady overland flow on flat surfaces induced by spatial permeability contrasts," Adv. Water Resour. 34, 1049–1058 (2011).
- ⁸A. B. de Saint-Venant, "Theorie du mouvement non permanent des eaux, avec application aux crues des rivieres et a l'introduction des mare es dans leurs lits," C. R. Seances Acad. Sci. **73**, 237–240 (1871).
- ⁹W. H. Hager, O. Castro-Orgaz, and K. Hutter, "Correspondence between de Saint-Venant and Boussinesq. 1: Birth of the shallow-water equations," C. R. Mec 347, 632-662 (2019).
- ¹⁰M. Lighthill and G. Whitham, "On kinematic waves. I. Flood movement in long rivers," Proc. R. Soc. London, Ser. A 229, 281–316 (1955).
- ¹¹R. H. French, Open-Channel Hydraulics (McGraw-Hill, New York, 1985).
- ¹²A. J. Hogg and D. Pritchard, "The effects of hydraulic resistance on dam-break and other shallow inertial flows," J. Fluid Mech. 501, 179–212 (2004).
- ¹³C. V. Bellos and J. G. Sakkas, "1-d dam-break flood-wave propagation on dry bed," J. Hydraul. Eng. 113, 1510–1524 (1987).
- 14 A. Ritter, "Die fortpflanzung der wasserwellen," Z. Ver. Dtsch. Ing. 36, 947–954 (1992)
- ¹⁵C. Ancey, R. Iverson, M. Rentschler, and R. Denlinger, "An exact solution for ideal dam-break floods on steep slopes," Water Resour. Res. 44, W01430, https://doi.org/10.1029/2007WR006353 (2008).

- ¹⁶H. Chanson, "Application of the method of characteristics to the dam break wave problem," J. Hydraul. Res. 47, 41–49 (2009).
- ¹⁷L. A. LaRocque, J. Imran, and M. H. Chaudhry, "Experimental and numerical investigations of two-dimensional dam-break flows," J. Hydraul. Eng. 139, 569–579 (2012).
- ¹⁸M. Melis, D. Poggi, O. D. Fasanella, Giovanni, S. Cordero, and G. G. Katul, "Resistance to flow on a sloping channel covered by dense vegetation following a dam break," Water Resour. Res. 55, 1040–1058, https://doi.org/10.1029/ 2018WR023889 (2019).
- ¹⁹H. Capart, "Analytical solutions for gradual dam breaching and downstream river flooding," Water Resour. Res. 49, 1968–1987, https://doi.org/10.1002/ wrcr.20167 (2013).
- ²⁰S. Kocaman and H. Ozmen-Cagatay, "The effect of lateral channel contraction on dam break flows: Laboratory experiment," J. Hydrol. 432-433, 145-153 (2012).
- ²¹S. Kocaman, H. Güzel, S. Evangelista, H. Ozmen-Cagatay, and G. Viccione, "Experimental and numerical analysis of a dam-break flow through different contraction geometries of the channel," Water 12, 1124 (2020).
- ²²L. Cozzolino, V. Pepe, F. Morlando, L. Cimorelli, A. D'Aniello, R. Della Morte, and D. Pianese, "Exact solution of the dam-break problem for constrictions and obstructions in constant width rectangular channels," J. Hydraul. Eng. 143, 04017047 (2017).
- ²³A. Ferdowsi, M. Nemati, and S. Farzin, "Development of dam-break model considering real case studies with asymmetric reservoirs," Comput. Eng. Phys. Model. 4, 39–63 (2021).
- ²⁴B. Wang, J. Zhang, Y. Chen, Y. Peng, X. Liu, and W. Liu, "Comparison of measured dam-break flood waves in triangular and rectangular channels," J. Hydrol. 575, 690–703 (2019).
- ²⁵W.-J. Wang, W.-X. Huai, Y.-H. Zeng, and J.-F. Zhou, "Analytical solution of velocity distribution for flow through submerged large deflection flexible vegetation," Appl. Math. Mech-Engl. Ed. 36, 107–120 (2015).
- ²⁶B. Wang, X. Liu, J. Zhang, Y. Guo, Y. Chen, Y. Peng, W. Liu, S. Yang, and F. Zhang, "Analytical and experimental investigations of dam-break flows in triangular channels with wet-bed conditions," J. Hydraul. Eng. 146, 04020070 (2020).
- ²⁷L.-H. Wang and C.-H. Pan, "An analysis of dam-break flow on slope," J. Hydrodyn. 26, 902–911 (2015).
- ²⁸S. S. Frazão and Y. Zech, "Dam break in channels with 90° bend," J. Hydraul. Eng. 128, 956–968 (2002).
- ²⁹R. F. Dressler, Hydraulic Resistance Effect upon the Dam-Break Functions (National Bureau of Standards, Washington, DC, 1952),Vol. 49, pp. 217–225.
- 30B. Hunt, "Perturbation solution for dam-break floods," J. Hydraul. Eng. 110, 1058–1071 (1984).
- ³¹B. Hunt, "Dam-break solution," J. Hydraul. Eng. **110**, 675–686 (1984).
- ³²P. Nielsen, B. Xu, D. Wüthrich, and S. Zhang, "Friction effects on quasi-steady dam-break wave propagation on horizontal beds," J. Fluid Mech. 939, A21 (2022).
- 33 R. Manning, "On the flow of water in open channels and pipes," Trans. Inst. Civil Eng. Ireland 20, 161–207 (1891).
- 34T. V. Chow, Open Channel Hydraulics (The Blackburn Press, Caldwell, NJ, 1959) p. 788.
- ³⁵G. Gioia and F. A. Bombardelli, "Scaling and similarity in rough channel flows," Phys. Rev. Lett. 88, 014501 (2001).
- 36S. Bonetti, G. Manoli, C. Manes, A. Porporato, and G. G. Katul, "Manning's formula and Strickler's scaling explained by a co-spectral budget model," J. Fluid Mech. 812, 1189–1212 (2017).
- ³⁷D. A. Woolhiser and J. A. Liggett, "Unsteady, one-dimensional flow over a plane: The rising hydrograph," Water Resour. Res. 3, 753–771, https://doi.org/ 10.1029/WR003i003p00753 (1967).
- 38H. Ozmen-Cagatay and S. Kocaman, "Dam-break flow in the presence of obstacle: Experiment and CFD simulation," Eng. Appl. Comput. Fluid Mech. 5, 541–552 (2011).
- 39S. Soares-Frazão and Y. Zech, "Dam-break flow through an idealised city," J. Hydraul. Res. 46, 648–658 (2008).
- ⁴⁰A. Del Gaudio, F. De Paola, C. Di Cristo, A. Leopardi, A. Vacca, and G. La Forgia, "Experimental investigation and numerical evaluation of the free surface of a dam break wave in the presence of an obstacle," Environ. Sci. Proc. 21, 23 (2022).

- ⁴¹C. Di Cristo, M. Greco, M. Iervolino, and A. Vacca, "Interaction of a dam-break wave with an obstacle over an erodible floodplain," J. Hydroinf. 22, 5–19 (2020).
- ⁴²M. M. Kamra, J. Al Salami, M. Sueyoshi, and C. Hu, "Experimental study of the interaction of dambreak with a vertical cylinder," J. Fluids Struct. 86, 185–199 (2019)
- 43A. Ansari, E. Khavasi, and J. Ghazanfarian, "Experimental and SPH studies of reciprocal wet-bed dam-break flow over obstacles," Int. J. Mod. Phys. C 32, 2150098 (2021)
- ⁴⁴F. Vosoughi, M. R. Nikoo, G. Rakhshandehroo, J. F. Adamowski, and A. H. Gandomi, "Downstream semi-circular obstacles' influence on floods arising from the failure of dams with different levels of reservoir silting," Phys. Fluids 34, 013312 (2022).
- ⁴⁵S. Kocaman, S. Evangelista, G. Viccione, and H. Güzel, "Experimental and numerical analysis of 3D dam-break waves in an enclosed domain with a single oriented obstacle," Environ. Sci. Proc. 2, 35 (2020).
- ⁴⁶Z. Huo and H. Liu, "Experimental study of the surge-and bore-induced impact pressure on a vertical wall and its foundation," Phys. Fluids 35, 016602 (2023).
- 47T. Tan, Y. Ma, J. Zhang, X. Niu, and K.-A. Chang, "Experimental study on flow kinematics of dam-break induced surge impacting onto a vertical wall," Phys. Fluids 35, 025127 (2023).
- ⁴⁸P. Stansby, A. Chegini, and T. Barnes, "The initial stages of dam-break flow," J. Fluid Mech. 374, 407–424 (1998).
- ⁴⁹H. Ozmen-Cagatay and S. Kocaman, "Dam-break flows during initial stage using SWE and RANS approaches," J. Hydraul. Res. 48, 603–611 (2010).
- 50 L. Espartel and R. Manica, "Experiments on initial stages of development of dam-break waves," Braz. J. Water Resour. 26, e6, https://doi.org/10.1590/2318-0331.262120200106 (2021).
- ⁵¹I. M. Jánosi, D. Jan, K. G. Szabó, and T. Tél, "Turbulent drag reduction in dambreak flows," Exp. Fluids 37, 219–229 (2004).
- ⁵²C. Di Cristo, S. Evangelista, M. Greco, M. Iervolino, A. Leopardi, and A. Vacca, "Dam-break waves over an erodible embankment: Experiments and simulations," J. Hydraul. Res. 56, 196–210 (2018).
- ⁵³K. E. K. Abderrezzak, A. Paquier, and B. Gay, "One-dimensional numerical modelling of dam-break waves over movable beds: Application to experimental and field cases," Environ. Fluid Mech. 8, 169–198 (2008).
- 54Y. Zech, S. Soares-Frazão, B. Spinewine, and N. Le Grelle, "Dam-break induced sediment movement: Experimental approaches and numerical modelling," J. Hydraul. Res. 46, 176–190 (2008).
- 55F. Vosoughi, G. Rakhshandehroo, M. R. Nikoo, and M. Sadegh, "Experimental study and numerical verification of silted-up dam break," J. Hydrol. 590, 125267 (2020).
- 56S. Biswal, M. Moharana, and A. Agrawal, "Effects of initial stage of dam-break flows on sediment transport," Sādhanā 43(12), 203 (2018).
- ⁵⁷K. Khosravi, A. H. N. Chegini, J. Cooper, L. Mao, M. Habibnejad, K. Shahedi, and A. Binns, "A laboratory investigation of bed-load transport of gravel sediments under dam break flow," Int. J. Sediment Res. 36, 229–234 (2021).
- ⁵⁸I. Fent, Y. Zech, and S. Soares-Frazão, "Dam-break flow experiments over mobile bed: Velocity profile," J. Hydraul. Res. 57, 131–138 (2019).
- ⁵⁹H. Qian, Z. Cao, H. Liu, and G. Pender, "New experimental dataset for partial dam-break floods over mobile beds," J. Hydraul. Res. 56, 124–135 (2018).
- ⁶⁰H. Nepf, "Drag, turbulence, and diffusion in flow through emergent vegetation," Water Resour. Res. 35, 479–489, https://doi.org/10.1029/1998WR900069 (1999).
- ⁶¹F. Wu, H. Shen, and Y. Chou, "Variation of roughness coefficients for unsub-merged and submerged vegetation," J. Hydraul. Eng. 125, 934–942 (1999).
- 62D. Lawrence, "Hydraulic resistance in overland flow during partial and marginal surface inundation: Experimental observations and modeling," Water Resour. Res. 36, 2381–2393, https://doi.org/10.1029/2000WR900095 (2000).
- ⁶³J. C. Green, "Modelling flow resistance in vegetated streams: Review and development of new theory," Hydrol. Processes 19, 1245–1259 (2005).
- ⁶⁴F. Huthoff, D. Augustijn, and S. J. Hulscher, "Analytical solution of the depth-averaged flow velocity in case of submerged rigid cylindrical vegetation," Water Resour. Res. 43, W06413, https://doi.org/10.1029/2006WR005625 (2007).
- ⁶⁵D. Poggi, C. Krug, and G. G. Katul, "Hydraulic resistance of submerged rigid vegetation derived from first-order closure models," Water Resour. Res. 45, W10442, https://doi.org/10.1029/2008WR007373 (2009).

- ⁶⁶W.-X. Huai, Y.-H. Zeng, Z.-G. Xu, and Z.-H. Yang, "Three-layer model for vertical velocity distribution in open channel flow with submerged rigid vegetation," Adv. Water Resour. 32, 487–492 (2009).
- ⁶⁷U. C. Kothyari, K. Hayashi, and H. Hashimoto, "Drag coefficient of unsubmerged rigid vegetation stems in open channel flows," J. Hydraul. Res. 47, 691–699 (2009).
- ⁶⁸H. M. Nepf, "Flow and transport in regions with aquatic vegetation," Annu. Rev. Fluid Mech. 44, 123–142 (2012).
- ⁶⁹V. Etminan, R. J. Lowe, and M. Ghisalberti, "A new model for predicting the drag exerted by vegetation canopies," Water Resour. Res. 53, 3179–3196, https://doi.org/10.1002/2016WR020090 (2017).
- 70Y. Tanino and H. M. Nepf, "Laboratory investigation of mean drag in a random array of rigid, emergent cylinders," J. Hydraul. Eng. 134, 34-41 (2008)
- ⁷¹T. Stoesser, S. Kim, and P. Diplas, "Turbulent flow through idealized emergent vegetation," J. Hydraul. Eng. 136, 1003–1017 (2010).
- 72]. Lee, L. Roig, H. Jenter, and H. Visser, "Drag coefficients for modeling flow through emergent vegetation in the Florida Everglades," Ecol. Eng. 22, 237–248 (2004).
- ⁷³N.-S. Cheng and H. T. Nguyen, "Hydraulic radius for evaluating resistance induced by simulated emergent vegetation in open-channel flows," J. Hydraul. Eng. 137, 995–1004 (2010).
- ⁷⁴M. M. Zdravkovich, Flow Around Circular Cylinders: Applications (Oxford University Press, Oxford, United Kingdom, 2000), Vol. 2.
- ⁷⁵D. Poggi, A. Porporato, L. Ridolfi, J. Albertson, and G. Katul, "The effect of vegetation density on canopy sub-layer turbulence," <u>Boundary-Layer Meteorol.</u> 111, 565–587 (2004).
- ⁷⁶N.-S. Cheng, "Calculation of drag coefficient for arrays of emergent circular cylinders with pseudofluid model," J. Hydraul. Eng. 139, 602–611 (2012).
- 77S. Belcher, N. Jerram, and J. Hunt, "Adjustment of a turbulent boundary layer to a canopy of roughness elements," J. Fluid Mech. 488, 369–398 (2003).
- 78W.-J. Wang, W.-X. Huai, S. Thompson, and G. G. Katul, "Steady nonuniform shallow flow within emergent vegetation," Water Resour. Res. 51, 10047– 10064, https://doi.org/10.1002/2015WR017658 (2015).

- ⁷⁹S. Singh and S. Mittal, "Flow past a cylinder: Shear layer instability and drag crisis," Numer. Methods Fluids 47, 75–98 (2005).
- 80 P. Wen and W. Qiu, "Investigation of drag crisis phenomenon using CFD methods," Appl. Ocean Res. 67, 306–321 (2017).
- ⁸¹I. Akkerman, Y. Bazilevs, D. Benson, M. Farthing, and C. Kees, "Free-surface flow and fluid-object interaction modeling with emphasis on ship hydrodynamics," J. Appl. Mech. 79, 010905 (2011).
- 82 S. Dai and S. Jin, "Numerical investigations of unsteady critical flow conditions over an obstacle using three models," Phys. Fluids 34, 025103 (2022).
- 83°C. Ai, Y. Ma, W. Ding, Z. Xie, and G. Dong, "Three-dimensional non-hydrostatic model for dam-break flows," Phys. Fluids 34, 022105 (2022).
- 84G. Hernández-Dueñas, M. A. Moreles, and P. González-Casanova, "Bathymetry and friction estimation from transient velocity data for onedimensional shallow water flows in open channels with varying width," Phys. Fluids 35, 027109 (2023).
- 85 I. Eames and T. Robinson, "Horizontal dam-break flow past a blocking-drag region," Phys. Fluids 34, 052104 (2022).
- 86X. Yan, R. Ao, A. Mohammadian, J. Liu, F. Du, and Y. Wang, "Fast mathematical modeling of partial-breach dam-break flow using a time-series field-reconstruction deep learning approach," Phys. Fluids 35, 043306 (2023).
- 87 Z. He, T. Wu, H. Weng, P. Hu, and G. Wu, "Numerical simulation of dambreak flow and bed change considering the vegetation effects," Int. J. Sediment Res. 32, 105–120 (2017).
- 88 A. Khoshkonesh, M. Daliri, K. Riaz, F. A. Dehrashid, F. Bahmanpouri, and S. Di Francesco, "Dam-break flow dynamics over a stepped channel with vegetation," J. Hydrol. 613, 128395 (2022).
- 89M-L. Zhang, Y.-Y Xu, Q. Yang, H.-Z. Jiang, Z.-Z. Zhang, and G.-S. Zhang, "Numerical simulation of flow and bed morphology in the case of dam break floods with vegetation effect," J. Hydrodyn. 28, 23–32 (2016).
- 90 A. Khoshkonesh, S. H. Sadeghi, S. Gohari, S. Karimpour, S. Oodi, and S. Di Francesco, "Study of dam-break flow over a vegetated channel with and without a drop," Water Resour. Manage. 37, 2107–2123 (2023).
- ⁹¹D. E. Alsdorf, E. Rodríguez, and D. P. Lettenmaier, "Measuring surface water from space," Rev. Geophys. 45, RG2002, https://doi.org/10.1029/2006RG000197